CrossMark

RESEARCH ARTICLE

Urchin-like α-FeOOH@MnO$_2$ core–shell hollow microspheres for high-performance supercapacitor electrode
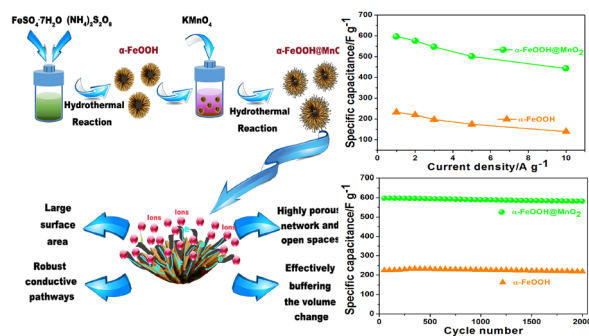
Yamei Lv[1] · Hongwei Che[1] · Aifeng Liu[1] · Jingbo Mu[1] · Chengxiang Dai[1] ·
Xiaoliang Zhang[1] · Yongmei Bai[1] · Guangshuo Wang[1] · Zhixiao Zhang[1]

Abstract This work details the design and synthesis of novel urchin-like α-FeOOH@MnO$_2$ core–shell hollow microspheres for high-performance electrode materials for supercapacitors. The core–shell heterostructures were constructed by growing strip-like MnO$_2$ nanostructures onto the urchin-like α-FeOOH hollow microspheres that were composed of nanorods. Based on the synergetic effects and multi-functionalities of both the MnO$_2$ shell and urchin-like α-FeOOH hollow cores, the resulting urchin-like α-FeOOH@MnO$_2$ core–shell hollow microspheres exhibited excellent electrochemical performance with a high specific capacitance of 597 F g^{-1} at 1 A g^{-1}, good rate capability (capacitance retention of 74.2% at 10 A g^{-1}), and remarkable cycling stability (capacitance retention of 97.1% after 2000 cycles). Moreover, an asymmetric supercapacitor fabricated using α-FeOOH@MnO$_2$ as positive electrode and activated carbon as negative electrode was found to deliver a high energy density of 34.2 W h kg^{-1} and power density of 815 W kg^{-1}.

Graphical Abstract Urchin-like α-FeOOH@MnO$_2$ hollow microspheres demonstrated a high specific capacitance, rate capability and cycling stability, suggesting its promising potential for high-performance supercapacitors.

1 Introduction

Supercapacitors (SCs) are attracting a great deal of research attention as a promising energy storage device based on their high power density, rapid rechargeability, long cycle lifetime, and low maintenance costs [1, 2]. It is well known that there are two types of SCs, electric double-layer capacitors (EDLCs) and pseudocapacitors (PCs), which are based on the charge storage mechanism [3]. Compared to EDLCs that employ carbon materials as electrodes, PCs that use transition metal oxides/hydroxides possess a higher capacitance and energy density as a result of a fast, reversible faradaic redox reaction [4]. Therefore, significant research attention has been focused on exploring the competitive transition metal oxides/hydroxides that have excellent capacitive characteristics such as RuO$_2$

✉ Hongwei Che
hongweiche@hebeu.edu.cn

✉ Aifeng Liu
liuaifeng@hebeu.edu.cn

[1] Department of Composite Materials and Engineering, College of Materials Science and Engineering, Hebei University of Engineering, Handan 056038, People's Republic of China

[5], MnO_2 [6–8], NiO [9, 10], $Ni(OH)_2$ [11, 12], Co_3O_4 [13–15], $Co(OH)_2$ [16, 17], and Fe_2O_3 [18, 19]. Although these metal oxides/hydroxides electrodes have a high theoretical specific capacitance, they often exhibit a specific capacitance that is lower than theoretical, as well as poor rate capacity and cycle stability. This is due to their poor electronic conductivity, limited contacting area with the electrolyte and serious structural deformation during the charge–discharge process. Therefore, to meet the demand for future high-performance SCs, it is highly desirable to design and synthesize better metal oxides/hydroxides electrodes that have a short ion transport/diffusion path, fast charge transfer, and intimate contact between the active materials and electrolyte.

Recently, composite electrode materials with core–shell heterostructures (CSHs) have been proven to exhibit excellent electrochemical performance compared to the individual components [20–22]. The CSHs where the core and shell are both active electrode materials can incorporate remarkable synergetic effects and multi-functionalities from the combination of the multiple components, including better electrical conductivity, shorter ionic transport path, higher contacting area, and improved mechanical stability. As a result, employing the composite electrode materials can produce a SC with high energy density, long cycling life, and high rate capability. Until now, a variety of CSHs including metal oxide@metal oxide [23–27] (e.g., $Co_3O_4@MnO_2$ [23]), metal oxide@conducting polymers [28, 29] (e.g., $\alpha\text{-}Fe_2O_3@PANI$ [28]) or carbon [30, 31] (e.g., CuO@C [31]), metal oxide@metal hydroxide [32–34] (e.g., $Co_3O_4@Ni(OH)_2$ [34]), and metal hydroxide@metal oxide [35, 36] (e.g., $Ni(OH)_2@Fe_2O_3$ [35]) have been synthesized and employed as electrode materials for SCs that have demonstrated improved electrochemical performance. Despite these efforts, further improvement in SC performance demands the development of novel, cost-effective materials such as high-performance core–shell composite electrode materials with well-defined morphologies and microstructures.

Herein, we report on the synthesis and electrochemical performance of novel urchin-like $\alpha\text{-}FeOOH@MnO_2$ core–shell hollow microspheres (CSMs) using a facile two-step hydrothermal method. As shown in Scheme 1, urchin-like $\alpha\text{-}FeOOH$ hollow microspheres composed of one-dimensional (1D) nanorods were initially prepared using a hydrothermal reaction. Then, 1D strip-like MnO_2 nanostructures were grown on the surfaces of $\alpha\text{-}FeOOH$ hollow microspheres to form $\alpha\text{-}FeOOH@MnO_2$ CSHs. Finally, the resulting urchin-like $\alpha\text{-}FeOOH@MnO_2$ CSHs were used as electrode materials for SCs to determine their electrochemical performance. It should be noted that although pristine FeOOH [37–40] and MnO_2 [6–8] with various morphologies and microstructures have been studied as electrode materials for SCs, there are no reports of the $\alpha\text{-}FeOOH@MnO_2$ CSHs used as electrode materials. The designed urchin-like $\alpha\text{-}FeOOH@MnO_2$ CSMs in the present study were expected to have improved electrochemical performance based on the combination of the properties of the $\alpha\text{-}FeOOH$ core and the MnO_2 shell. It was believed this would occur, because first, both the core and shell are good

Scheme 1 Schematic illustration of the preparation of the urchin-like $\alpha\text{-}FeOOH@MnO_2$ hollow microspheres and its structural merits in electrochemical energy storage
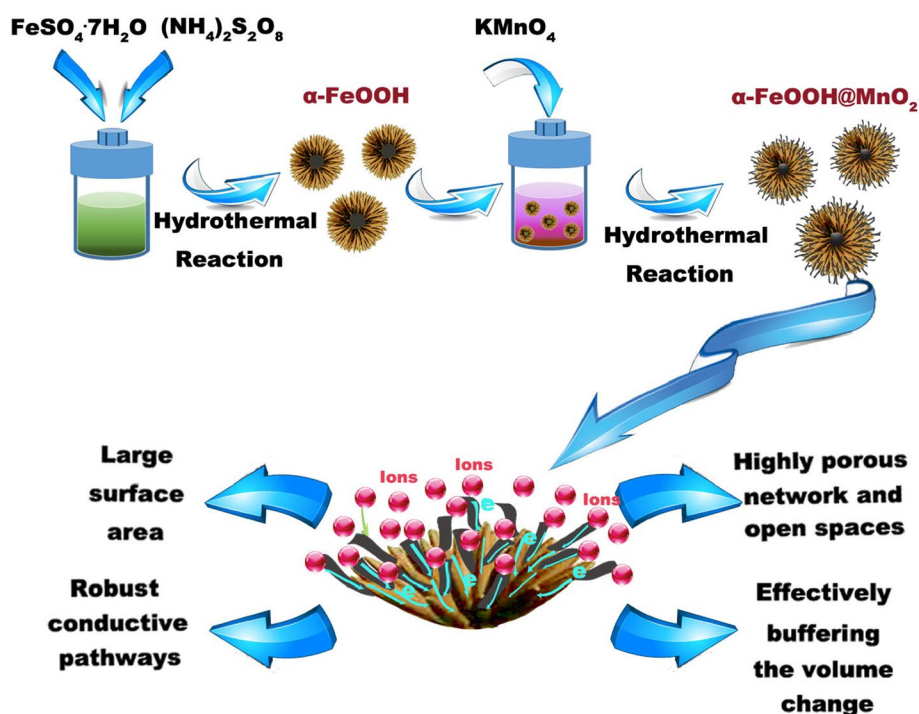
PC materials with high theoretical capacity, which would contribute to a high total specific capacitance. Second, the 1D strip-like MnO_2 nanostructures were grown on the surface of α-FeOOH nanorods, which helped to increase the surface area of the α-FeOOH@MnO_2 electrode. In addition, the strip-like MnO_2 nanostructures shell were well separated, providing open spaces, which ensured that both the shell and core would be fully accessible by the electrolyte. Third, the hollow interior of the urchin-like α-FeOOH core and the well dispersed strip-like MnO_2 nanostructures shell can effectively buffer the volume changes that occur during the charge/discharge process, which would increase the cycling stability. Fourth, strip-like MnO_2 nanostructures and α-FeOOH nanorods are intimately connected, which results in low contact resistance and forms rich and fast electronic transport pathways. Finally, both the core and shell are naturally abundant materials, which are low cost and environmentally benign. Based on these advantages, it was found that the novel α-FeOOH@MnO_2 core–shell electrode materials demonstrated high specific capacitance, good rate capability and excellent cycle stability.

2 Experimental section

2.1 Synthesis of urchin-like α-FeOOH hollow microspheres

All of the reagents were analytical grade and used without further purification. Typically, 0.42 g (1.5 mmol) of $FeSO_4 \cdot 7H_2O$ was dissolved in 30 ml deionized water at 30 °C. Then, 0.22 g of $(NH_4)_2S_2O_8$ was added under stirring. The obtained transparent solution was transferred and sealed in a 50-ml Teflon-lined stainless autoclave. The autoclave was heated to 140 °C for 10 h, then cooled to room temperature. The yellowish-brown products were collected by filtration, washed with deionized water and ethanol, and dried in a vacuum at 60 °C for 12 h.

The formation reaction of α-FeOOH can be described in the following step:

$$2Fe^{2+} + S_2O_8^{2-} + 4H_2O \rightarrow 2FeOOH\,(s) + 2SO_4^{2-} + 6H^+$$
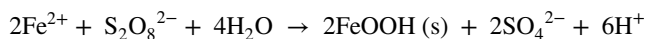
2.2 Synthesis of urchin-like α-FeOOH@MnO_2 CSMs

Typically, 30 mg of the as-prepared urchin-like α-FeOOH products were dispersed to 30 ml of $KMnO_4$ solution (30 mmol/l) by ultrasonication for 20 min. Then the mixture was put into a 50-ml Teflon-lined stainless autoclave, and subsequently maintained at 160 °C for 12 h. Finally, the sample was obtained by centrifugation, washed with deionized water and ethanol, and dried in a vacuum at 60 °C for 12 h.

The formation reaction of MnO_2 shell can be described in the following step:

$$4MnO_4^- + 2H_2O \rightarrow 4MnO_2(s) + 4OH^- + 3O_2$$

2.3 Characterization

X-ray diffraction (XRD) measurements were performed on a Rigaku Smartlab X-ray diffractometer. Field emission scanning electron microscopy (FESEM) images were observed on a SU8200 field emission instrument with an energy dispersive X-ray spectrometer (EDS). High-resolution transmission electron microscopy (HRTEM) images were obtained using a FEI Tecnai G20 electron microscope operating at 200 kV. X-ray photoelectron spectroscopy (XPS, Kratos Amicus) was used to determine the cation oxidation states of the products. Nitrogen adsorption–desorption isotherms measurements were carried out at 77 K by a conventional volumetric technique with a Quantachrome NOVA3200e sorption analyser.

2.4 Electrochemical measurement

Typically, the obtained urchin-like α-FeOOH@MnO_2 CSMs, acetylene black, and polytetrafluoroethylene (PTFE) binder (weight ratio of 80:10:10) were homogeneously blended with a few drops of ethanol in an agate mortar. Then the resulting paste was coated onto a nickel foam (1 cm^2) and pressed under a pressure of 10 MPa. The used electrolyte was 2 M KOH aqueous solution. The capacitive performance of the samples was measured on a CHI 660E (Shanghai Chenhua Co. Ltd, China) electrochemical workstation. Cyclic voltammetry (CV), galvanostatic charge–discharge (GCD) performances, and electrochemical impedance spectroscopy (EIS) measurements were tested with a three-electrode cell in which Pt wire serves as the counter electrode and a saturated calomel electrode (SCE) as the reference electrode. The specific capacitance of the electrodes at different current densities was calculated using $C = (I \times \Delta t)/(m \times \Delta V)$, where C (F g^{-1}) is the specific capacitance, I (A) is the discharge current, Δt (s) is the discharge time, ΔV is the voltage interval, and m (g) is the mass of the active material.

2.5 Fabrication of an asymmetric supercapacitor

The asymmetric SC cell (ASC) was assembled via using the urchin-like α-FeOOH@MnO_2 CSMs electrode as the positive electrode and active carbon (AC) as the negative electrode in a 2 M KOH aqueous solution. The ASC electrodes were separated by a cellulose paper separator. Moreover, to obtain the best performance of the ASC, the loading mass ratio of the negative and positive electrodes was calculated to be 0.8 based on the specific capacitance values of two electrodes

and their corresponding potential windows according to the following equations:

$$q^+ = q^- \tag{1}$$

$$q = m \times C \times \Delta V \tag{2}$$

$$m^+/m^- = (C^- \times \Delta V^-)/(C^+ \times \Delta V^+) \tag{3}$$

The power (P) and energy (E) densities of the ASC are calculated using the given equation:

$$E = \frac{1}{2} C \times (\Delta V)^2 \tag{4}$$

$$P = \frac{E}{\Delta t} \tag{5}$$

3 Results and discussion

Figure 1a displays the typical XRD patterns of the synthesized α-FeOOH and α-FeOOH@MnO$_2$ products. As shown in Fig. 1a, all the diffraction peaks can be indexed to orthorhombic α-FeOOH (JCPDS no. 29–0713), indicating that the synthesized product was composed of pure α-FeOOH. Compared with pure α-FeOOH, the synthesized α-FeOOH@MnO$_2$ composite products exhibited two new diffraction peaks at 12.4° and 24.6° as shown in Fig. 1b. The two new peaks were attributed to the (001) and (002) planes of birnessite-type δ-MnO$_2$ (JCPDS no. 80-1098), which confirmed the co-existence of α-FeOOH and δ-MnO$_2$ in the resulting composite products.

XPS measurements were performed on the products to determine the oxidation state of the Fe and Mn elements in the α-FeOOH@MnO$_2$ product, and the corresponding results are shown in Fig. 1(b–d). Figure 1b shows the high-resolution Fe 2p spectrum, where two peaks at around 711.2 and 724.9 eV can be attributed to Fe 2p$_{3/2}$ and Fe 2p$_{1/2}$ of Fe^{3+} ions from FeOOH [41, 42]. Also, the
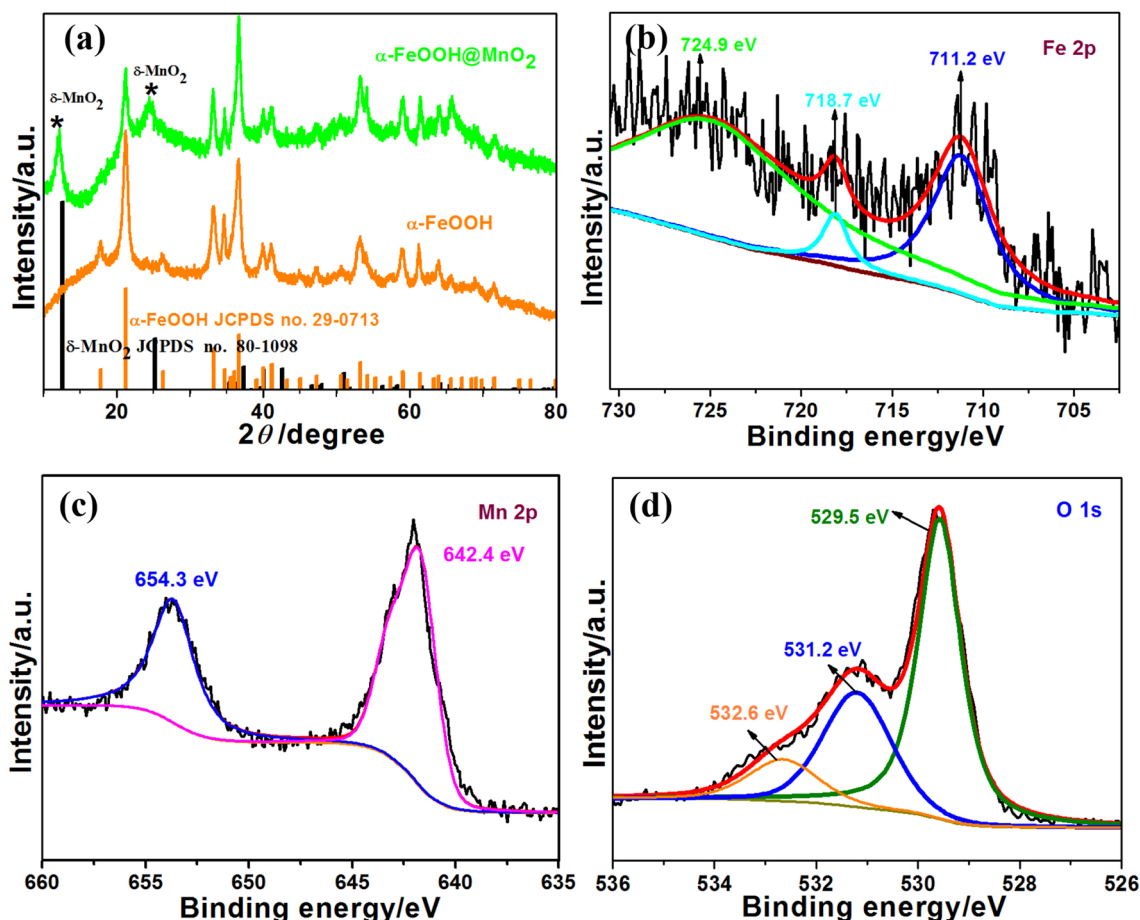

Fig. 1 a XRD patterns of the as-prepared α-FeOOH and α-FeOOH@MnO$_2$ products. High-resolution XPS spectra of (b) Fe 2p spectrum, c Mn 2p spectrum, and d O 1 s spectrum in the as-prepared α-FeOOH@MnO$_2$ product

corresponding satellite peak of Fe $2p_{3/2}$ is located at around 718.7 eV, further confirming the presence of Fe^{3+} ions in the composite products [41, 42]. The high-resolution Mn 2p spectrum in Fig. 1c exhibits two peaks at 642.4 and 654.3 eV, which correspond to Mn $2p_{3/2}$ and Mn $2p_{1/2}$, [24, 26]. The gap value of the binding energies was about 12 eV, confirming the presence of Mn^{4+} ions from MnO_2 in the composite products [24, 26]. Moreover, in the high-resolution O 1 s spectrum (Fig. 1d), three peaks at 529.5, 531.2, and 532.6 eV were assigned to the metal–oxygen

bonds (Fe–O and Mn–O), metal-hydroxyl bond (Fe–OH), and adsorbed surface hydroxyl groups (–OH) [40]. These XPS results indicate that the α-FeOOH@MnO_2 composite products had a mixed microstructure composition containing Fe^{3+}, Mn^{4+}, and O^{2-} species.

The morphology of the prepared α-FeOOH and α-FeOOH@MnO_2 products was investigated using SEM analysis. As shown in Fig. 2a, the prepared α-FeOOH products were composed of urchin-like microspheres with diameters of 1–2 μm. These microspheres were constructed

Fig. 2 Typical SEM images of the as-prepared α-FeOOH (**a, b**) and α-FeOOH@MnO_2 products (**c, d**); Element mappings of total elements (**e**), O (**f**), Mn (**g**), and Fe (**h**)
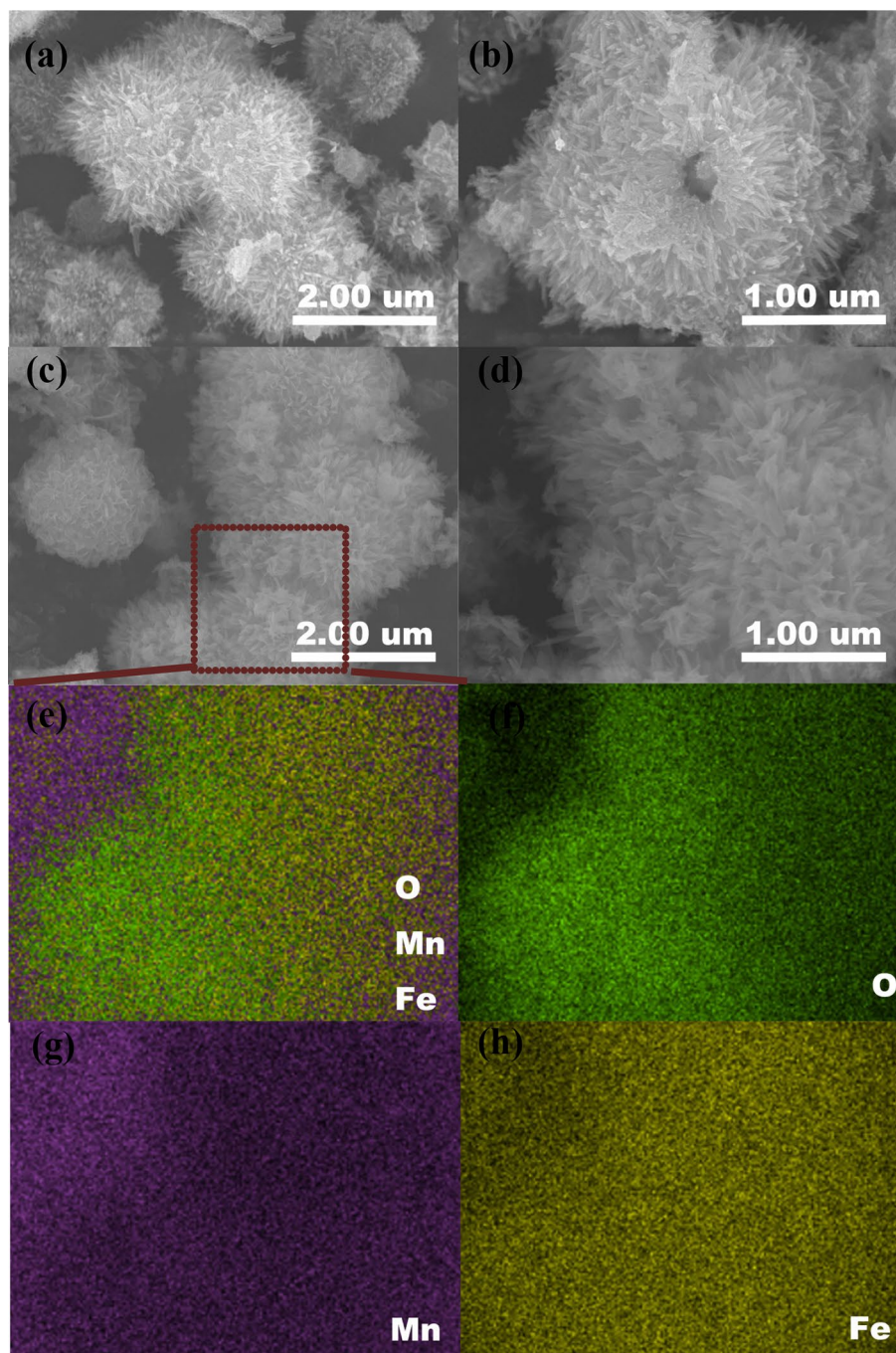
from numerous nanorods that were radially aligned from their common center. Furthermore, as depicted by a broken microsphere (Fig. 2b), the core of the urchin-like microsphere was hollow.

Figure 2c shows the SEM image of the prepared α-FeOOH@MnO$_2$ products. Similar to the α-FeOOH product, the urchin-like microsphere structure was apparent, but the diameters of the composite microspheres increased to 2–3 µm over that of the urchin-like α-FeOOH microspheres. Moreover, the enlarged SEM image of the composite material (Fig. 2d) shows that the surface of these urchin-like microspheres consisted of flexible strip-like nanostructures, which is obviously different from the nanorods that were grown radially on the surface of the urchin-like α-FeOOH microspheres. The EDS mapping images (Fig. 2e–h) in a select region from the urchin-like α-FeOOH@MnO$_2$ microspheres indicated that the elements Fe and O were are homogeneously distributed throughout, while Mn was dominant on the surface of this select region, as confirmed by the hollow shape in this region. Therefore, it can be inferred that the strip-like MnO$_2$ nanostructures grew on the surface of the urchin-like α-FeOOH to form

a core–shell α-FeOOH@MnO$_2$ structure. Moreover, the spectral data for the urchin-like α-FeOOH@MnO$_2$ microspheres indicated that the atomic ratio of Mn/Fe on the surface (Fig. S1, Supporting Information) was 0.80.

TEM analysis was performed on the products to further confirm the microstructure of the urchin-like α-FeOOH@ MnO$_2$ microspheres. Figure 3a shows the obvious nature of the hollow microstructures, which was in agreement with the results of the SEM analysis. The features of core–shell microstructure can be identified by the significant contrast between the core and shell. The enlarged TEM image (Fig. 3b, c) shows that the shell was composed of strip-like nanostructures with widths of 10–20 nm. The corresponding HRTEM image (Fig. 3d) of the shell shows clear lattice spacings of 0.69 nm, which reflected the interplanar distance of the (001) plane of the MnO$_2$. This further confirmed that the shell was composed of a MnO$_2$ crystal phase, which agreed well with the XRD patterns presented in Fig. 1.

Figure 4a, b show the nitrogen adsorption–desorption isotherms and the corresponding pore size distribution curves of the prepared urchin-like α-FeOOH

Fig. 3 TEM images of the as-prepared α-FeOOH@MnO$_2$ products (**a**–**c**) and the corresponding HRTEM image (**d**)
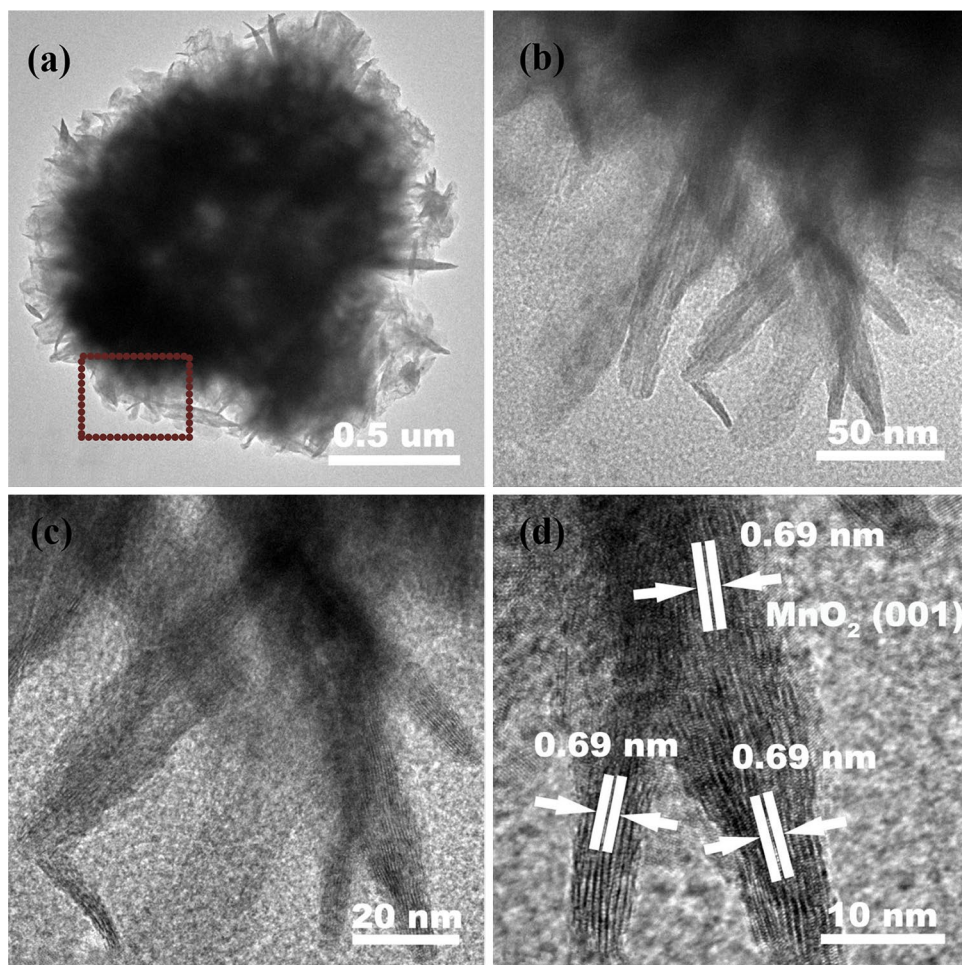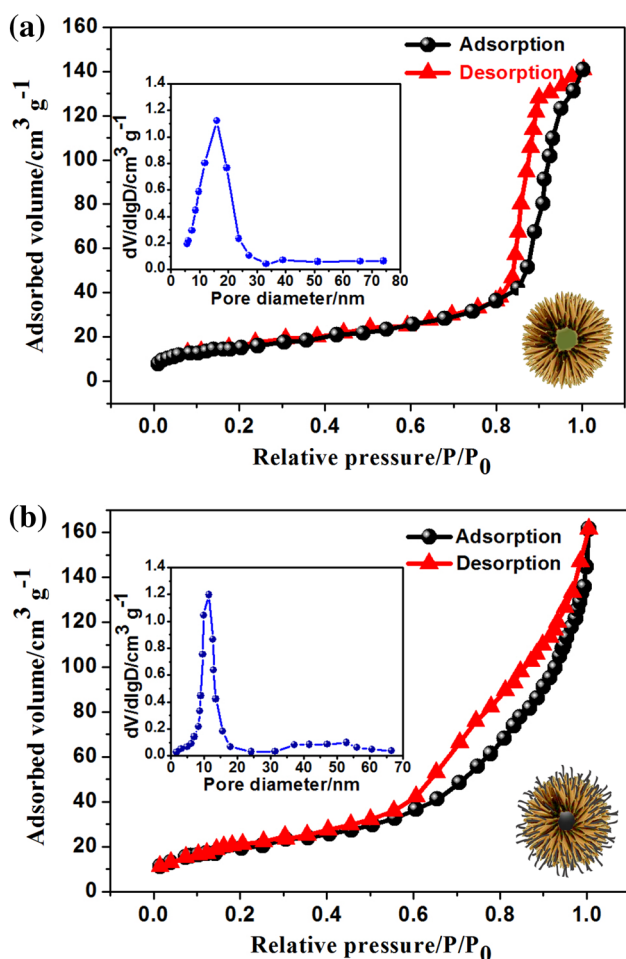
Fig. 4 Nitrogen adsorption–desorption isotherms of the as-prepared α-FeOOH (**a**) and α-FeOOH@MnO$_2$ products (**b**). The insets show the corresponding BJH pore size distribution plots

and α-FeOOH@MnO$_2$ products. Two pairs of isotherms can be classified as type IV with characteristic hysteresis loops at around P/P$_0$ of 0.6-1.0, suggesting the existence of mesopores in the α-FeOOH and α-FeOOH@MnO$_2$ composite products. The corresponding Brunauer–Emmett–Teller (BET) specific areas calculated to be 40.1 and 76.3 m^2 g^{-1}. Therefore, the strip-like MnO$_2$ nanostructures grown on the α-FeOOH cores significantly increased the surface area of the α-FeOOH@MnO$_2$ composite products. As a result, it can be expected that the electrochemical performance of the α-FeOOH@MnO$_2$ products will be superior to the α-FeOOH as a result of the enhanced contact area between the electrolyte and electrode. Moreover, the Barrett–Joyner–Halenda (BJH) pore size distribution curves from the adsorption branches in the insets in Fig. 4a, b show that the BJH pore sizes of the α-FeOOH and α-FeOOH@MnO$_2$ composite products were centered at 16.1 and 11.3 nm.

The electrochemical performance of the urchin-like α-FeOOH and α-FeOOH@MnO$_2$ products when employed as electrode materials was evaluated and compared in a three-electrode system using 2 M KOH aqueous electrolyte. Figure 5a shows the CV curves of the urchin-like α-FeOOH@MnO$_2$ electrode at various scan rates of 10–50 mV s^{-1}. Well-fined redox peaks in a potential window of 0-0.5 V (vs. SCE) were clearly displayed for the two electrodes, indicating their faradaic redox behavior. The redox reactions result from the reversible conversion of FeOOH/FeO [37] and MnO$_2$/MnOOK [6, 43] in KOH aqueous solution. Figure 5b shows the comparative CV curves of the urchin-like α-FeOOH@MnO$_2$ and the pristine urchin-like α-FeOOH electrodes at a scan rate of 50 mV s^{-1}. The current density and area of the CV curve of the urchin-like α-FeOOH@MnO$_2$ electrode were significantly larger than the pristine urchin-like α-FeOOH electrode, meaning that the α-FeOOH@MnO$_2$ electrode possessed a higher specific capacitance than the unmodified α-FeOOH electrode. Similar results have also been reported for the superior electrochemical performances of core–shell Co$_3$O$_4$@MnO$_2$ [23], CuO@MnO$_2$ [24], NiO@ MnO$_2$ [25], and NiCo$_2$O$_4$@MnO$_2$ [26] composites electrodes used in SCs. Figure 5c displays the GCD curves of the urchin-like α-FeOOH@MnO$_2$ electrodes over a potential range of 0–0.45 V at a current density of 1–10 A g^{-1}. The GCD curve of the pristine α-FeOOH electrode is also presented in Fig. S2 (see Supporting Information). From these results, it can be seen that both GCD curves exhibited obvious voltage plateaus, which further confirmed the good electrochemical capacitive behavior of the faradaic redox reaction. The corresponding specific capacitance was calculated and is presented in Fig. 5d. As shown, the urchin-like α-FeOOH@MnO$_2$ electrode exhibited more capacitance than the pristine urchin-like α-FeOOH electrode at all current densities. This result is consistent with the analysis of the CV results. At a current density of 1 A g^{-1}, the specific capacitance of the urchin-like α-FeOOH@MnO$_2$ and pristine α-FeOOH electrodes were calculated as 597 and 232 F g^{-1}. When the current density was increased to 10 A g^{-1}, the corresponding capacity retention was calculated to be 74.2% for the urchin-like α-FeOOH@MnO$_2$ electrode and 60.0% for the pristine α-FeOOH electrode, indicating that the urchin-like α-FeOOH@MnO$_2$ electrode also possessed better rate capability than the pristine urchin-like α-FeOOH electrode. Moreover, the cycling stability of the two electrodes was also evaluated by GCD at a current density of 1 A g^{-1} over 2000 cycles as shown in Fig. 5e. It can be seen that after 2000 cycles, the urchin-like α-FeOOH@MnO$_2$ electrode exhibited a capacitance retention of 97.1%, which was higher than 93.2% of the pristine urchin-like α-FeOOH electrode. Also, by comparison, the electrochemical performance of the as-prepared
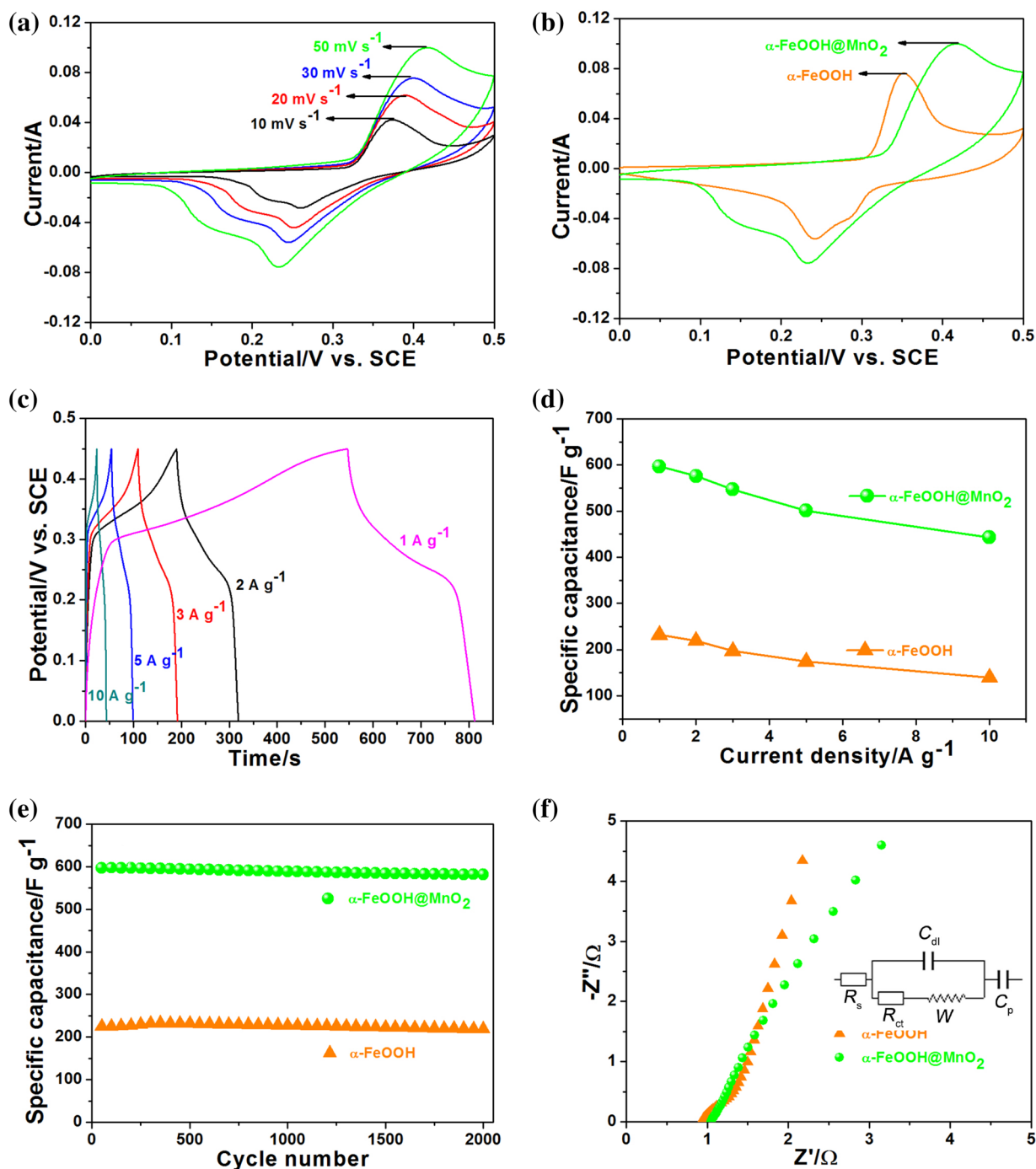
Fig. 5 **a** CV curves of the α-FeOOH@MnO$_2$ electrode at different scan rates of 10–50 mV s^{-1}. **b** Comparison of CV curves of the urchin-like α-FeOOH@MnO$_2$ and pristine urchin-like α-FeOOH electrodes at a scan rate of 50 mV s^{-1}. **c** Galvanostatic charge–discharge curves of the α-FeOOH@MnO$_2$ electrode at different current densities of 1–10 A g^{-1}. **d** Comparison of specific capacitances at different current densities of 1–10 A g^{-1}, **e** Cycling performance after 2000 cycles at 1 A g^{-1}, and **f** Nyquist plots (*inset* shows the equivalent *circuit diagram*) in the frequency range of 0.01–10^5 Hz of the urchin-like α-FeOOH@MnO$_2$ and pristine urchin-like α-FeOOH electrodes

α-FeOOH@MnO$_2$ electrode in this reported work was also superior to that reported for single or core–shell transition metal oxides or hydroxides (Table 1 in Supporting Information).

The enhanced specific capacitance, rate capability, and cycling stability of the urchin-like α-FeOOH@MnO$_2$ electrode can be attributed to the features of its core–shell heterostructure. Specifically, first, the formation of CSHs

contributes to increased specific area, which was confirmed by the BET surface area analysis. So, greater contact area with the electrolyte can be obtained, resulting in an enhanced specific capacitance. Second, the 1D nanostructures of both the core and shell offer the advantages of a high aspect ratio and directional electron pathways compared with other nanostructures. This shortens the diffusion and migration pathways which facilitates fast transport of ions and electrons. These features are of great significance in the enhancement of the rate capability of the urchin-like α-FeOOH@MnO$_2$ electrode. Third, the well dispersed strip-like MnO$_2$ shell can prevent the urchin-like α-FeOOH cores from agglomerating and the hollow interiors of the α-FeOOH cores can also effectively accommodate the volume changes that occur during the charge–discharge process. Consequently, good cycling stability can be obtained.

The improved electrochemical performance of the urchin-like α-FeOOH@MnO$_2$ electrode was further elucidated using electrochemical impedance spectroscopy (EIS). As shown in Fig. 5f (the inset is the equivalent circuit diagram), the shapes of the Nyquist plots for the two electrodes consisted of one semicircle in the high-frequency region followed by one straight sloping line in the low-frequency region. The semicircle of the Nyquist plots is related to the Faradic reactions and its diameter corresponds to the interfacial charge transfer resistance (Rct). The straight sloping line in the low-frequency region is associated with the diffusion resistance (Warburg impendence, W) of the electrolyte into the interior part of the electrode. At low frequency, both the urchin-like α-FeOOH@MnO$_2$ electrode and the pristine urchin-like α-FeOOH electrode displayed a high slope in the line, which corresponds to facile and fast diffusion of electrolyte ions onto the surface of the electrodes. However, in the high-frequency region, the α-FeOOH@MnO$_2$ electrode exhibited a much smaller semicircle than the unmodified α-FeOOH electrode, which indicated improved ion and electron transport between the electrolyte and the electrode in the former. These results imply that facile ion diffusion as well as fast electron transport was responsible for improving the electrochemical performance of the urchin-like α-FeOOH@MnO$_2$ electrode.

To further explore the practical application of the urchin-like α-FeOOH@MnO$_2$ electrodes in SCs, an ASC device was assembled using the urchin-like α-FeOOH@MnO$_2$ and AC as the positive and negative electrodes, as shown in Fig. 6a. The active mass of the α-FeOOH@MnO$_2$ core–shell material was 2.0 mg and the AC material weighed 1.6 mg. The ASC was subjected to CV analysis at a scan rate of 10 mV s^{-1} to determine the potential window of the ASC. As shown in Fig. 6b, the ASC had an operation voltage of 1.6 V. The CV curves in Fig. 6c of the ASC measured within various potential windows further confirmed that the potential window of the ASC was 0–1.6 V.

Fig. 6d shows the curves of the ASC at different scan rates of 10–50 mV s^{-1} in a potential window of 0–1.6 V. All of these CV curves exhibited a quasi-rectangular shape with broad redox peaks, exhibiting a combination of both pseudocapacitive and dielectric EDLC behavior in the ASC device. Also, no clear changes were seen in the curves as the scan rate was increased suggesting good rate capability in the ASC device. Figure 6e shows that the GCD curves of the ASC were different at various current densities which corresponded to the specific capacitance data presented in Fig. 6 f. The specific capacitance of the ASC was 96.3 F g^{-1} at a current density of 1 A g^{-1} and remained at 69.4 F g^{-1} with a retention of 72% when the current density was enhanced to 10 A g^{-1}. The cycling stability of the ASC was also measured at 3 A g^{-1} for 2000 cycles. As shown in Fig. 6g, 94.2% of the initial capacitance remained. Figure 6h shows the Ragone plots of the ASC. The ASC exhibited a maximum energy density of 34.2 W h kg^{-1} at a power density of 815 W kg^{-1}. It delivered an energy density of 24.7 W h kg^{-1} at a power density of 7800 W kg^{-1}. The maximum energy density of the ASC was also significantly higher than or close to that of other reported ASCs such as MnO$_2$ nanotubes//AG (22.6 W h kg^{-1} at 225.3 W kg^{-1}) [7], CNFs/MnO$_2$//AC (20.3 W h kg^{-1} at 485 W kg^{-1}) [44], Co$_3$O$_4$@MnO$_2$ nanowires//MEGO (17.7 W h kg^{-1} at about 600 W kg^{-1}) [23], CuO@MnO$_2$ nanostructures//MEGO (22.1 W h kg^{-1} at about 260 W kg^{-1}) [24], NiO@MnO$_2$ nanosheets//AC (30.6 W h kg^{-1} at 400 W kg^{-1}) [25], NiCo$_2$O$_4$@MnO$_2$ nanowires//AC (35 W h kg^{-1} at 163 W kg^{-1}) [26], and MnO$_2$@Fe$_2$O$_3$ nanospindles//AC (43.8 W h kg^{-1} at 110 W kg^{-1}) [27]. Therefore, the above results confirm the potential of the urchin-like α-FeOOH@MnO$_2$//AC ASC in practical applications for SC energy storage.

4 Conclusions

In summary, we have successfully synthesized the urchin-like α-FeOOH@MnO$_2$ CSMs via a facile two-step hydrothermal method, in which strip-like MnO$_2$ nanostructures are grown on the surface of urchin-like α-FeOOH hollow microspheres to form the CSHs. The as-synthesized core–shell α-FeOOH@MnO$_2$ heterostructures as an electrode for SC demonstrated higher specific capacitance, rate capability, and cycling stability than the pristine urchin-like α-FeOOH hollow microspheres electrode. Such excellent capacitive behavior can be ascribed to the synergetic effects and multi-functionalities from both MnO$_2$ shell and urchin-like α-FeOOH hollow cores. Besides, the as-fabricated α-FeOOH@MnO$_2$//AC ASC also exhibits a high energy density and power density. Our results suggest that such α-FeOOH@MnO$_2$ heterostructures are promising
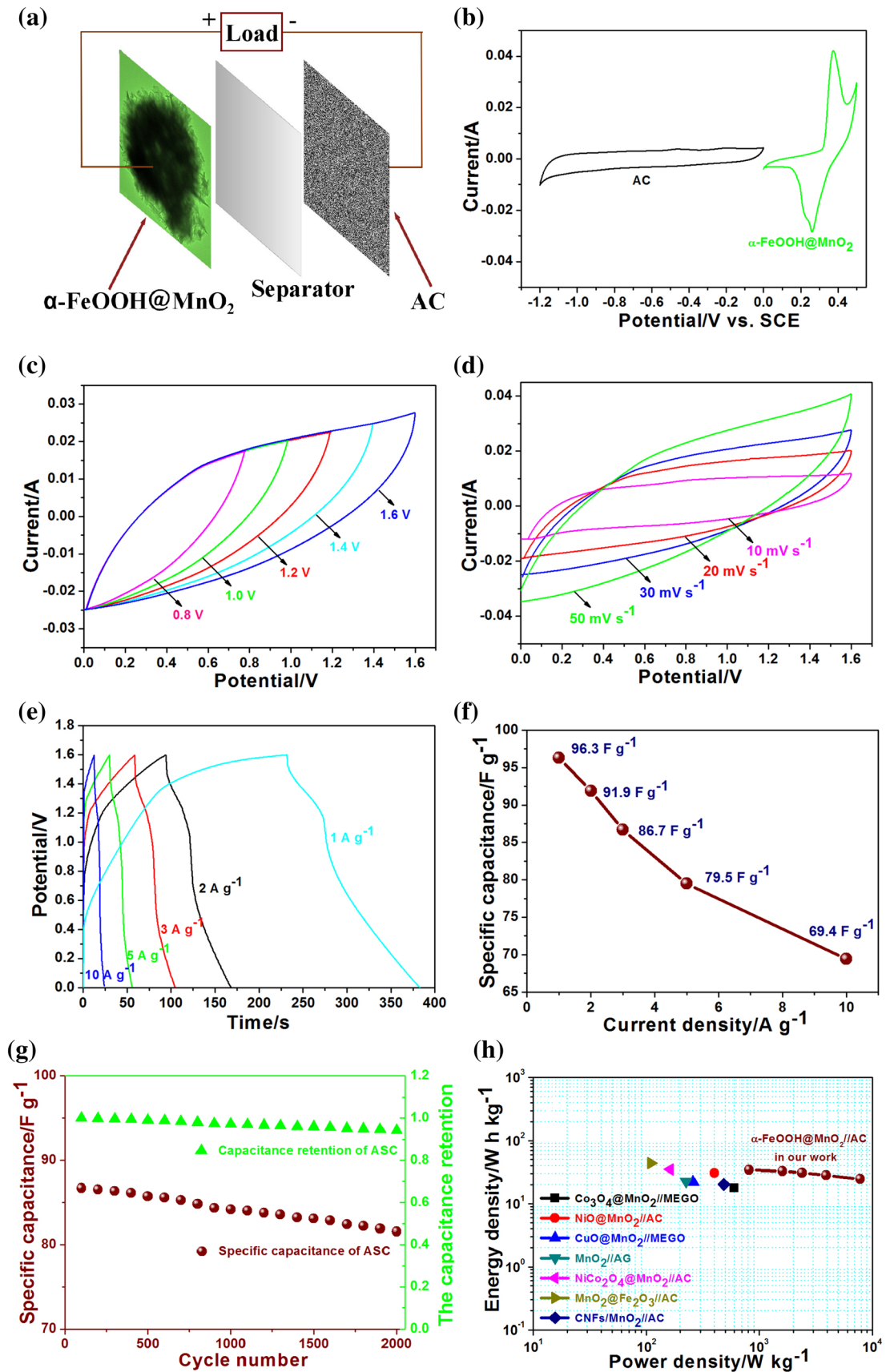
◄**Fig. 6 a** Schematic illustration of the as-fabricated α-FeOOH@ MnO₂//AC asymmetric supercapacitor. **b** CV curves of the α-FeOOH@MnO₂ and AC electrodes at a scan rate of 10 mV s⁻¹, **c** and **d** CV curves at different scan voltage windows at a scan rate of 30 mV s⁻¹ and at different scan rates, respectively, **e** Galvanostatic charge–discharge curves at different current densities, **f** Corresponding specific capacitance at different current densities, **g** Cycling performance after 2000 cycles at 3 A g⁻¹, and **h** Ragone plots and a comparison with the related references of the α-FeOOH@MnO₂// AC ASC

for high-performance SC, and our work also provides a rational design and facile synthesis strategy toward achieving advanced electrode materials with superior electrochemical performance for SCs.

References

1. Miller JR, Simon P (2008) Electrochemical capacitors for energy management. Science 321:651–652
2. Simon P, Gogotsi Y (2008) Materials for electrochemical capacitors. Nat Mater 7:845–854
3. Conway BE, Pell WG (2003) Double-layer and pseudocapacitance types of electrochemical capacitors and their applications to the development of hybrid devices. J Solid State Electr 7:637–644
4. Conway BE, Birss V, Wojtowicz J (1997) The role and utilization of pseudocapacitance for energy storage by supercapacitors. J Power Sources 66:1–14
5. Hu CC, Chang KH, Lin MC, Wu YT (2006) Design and tailoring of the nanotubular arrayed architecture of hydrous RuO₂ for next generation supercapacitors. Nano Lett 6:2690–2695
6. Wang JG, Kang F, Wei B (2015) Engineering of MnO₂-based nanocomposites for high-performance supercapacitors. Prog Mater Sci 74:51–124
7. Li F, Zhang YX, Huang M, Xing Y, Zhang LL (2015) Rational design of porous MnO₂ tubular arrays via facile and templated method for high performance supercapacitors. Electrochimi Acta 154:329–337.
8. Huang M, Li F, Dong F, Zhang YX, Zhang LL (2015) MnO₂-based nanostructures for high-performance supercapacitors. J Mater Chem A 3:21380–21423
9. Zheng X, Wang H, Wang C, Deng Z, Chen L, Li Y, Hasan T, Su BL (2016) 3D interconnected macro-mesoporous electrode with self-assembled NiO nanodots for high-performance supercapacitor-like Li-ion battery. Nano Energy 22:269–277
10. Babu GA, Ravi G, Mahalingam T, Kumaresavanji M, Hayakawad Y (2015) Influence of microwave power on the preparation of NiO nanoflakes for enhanced magnetic and supercapacitor applications. Dalton Trans 44:4485–4497
11. Dong X, Guo Z, Song Y, Hou M, Wang J, Wang Y, Xia Y (2014) Flexible and wire-shaped micro-supercapacitor based on Ni(OH)₂-nanowire and ordered mesoporous carbon electrodes. Adv Funct Mater 24:3405–3412
12. Jiang C, Zhao B, Cheng J, Li J, Zhang H, Tang Z, Yang J (2015) Hydrothermal synthesis of Ni(OH)₂ nanoflakes on 3D graphene foam for high-performance supercapacitors. Electrochimi Acta 173:399–407.
13. Zhang YZ, Wang Y, Xie YL, Cheng T, Lai WY, Pang H, Huang W (2014) Porous hollow Co₃O₄ with rhombic dodecahedral structures for high-performance supercapacitors. Nanoscale 6:14354–14359
14. Wang Y, Pan A, Zhu Q, Nie Z, Zhang Y, Tang Y, Liang S, Cao G (2014) Facile synthesis of nanorod-assembled multi-shelled Co₃O₄ hollow microspheres for high-performance supercapacitors. J Power Sources 272:107–112
15. Liao Q, Li N, Jin S, Yang G, Wang C (2015) All-solid-state symmetric supercapacitor based on Co₃O₄ nanoparticles on vertically aligned graphene. ASC Nano 9:5310–5317
16. Gao S, Sun Y, Lei F, Liang L, Liu J, Bi W, Pan B, Xie Y (2014) Ultrahigh energy density realized by a single-layer β-Co(OH)₂ all-solid-state asymmetric supercapacitor. Angew Chem 126:13003–13007
17. Wang Z, Liu Y, Gao C, Jiang H, Zhang J (2015) A porous Co(OH)₂ material derived from a MOF template and its superior energy storage performance for supercapacitors. J Mater Chem A 3:20658–20663
18. Zheng X, Han Z, Yao S, Xiao H, Chai F, Qu F, Wu X (2016) Spinous α-Fe₂O₃ hierarchical structures anchored on Ni foam for supercapacitor electrodes and visible light driven photocatalysts. Dalton Trans 45:7094–7103
19. Chaudhari NK, Chaudhari S, Yu JS (2014) Cube-like α-Fe₂O₃ supported on ordered multimodal porous carbon as high performance electrode material for supercapacitors. ChemSusChem 7:3102–3111
20. Xia X, Tu J, Zhang Y, Wang X, Gu C, Zhao X, Fan HJ (2012) High-quality metal oxide core/shell nanowire arrays on conductive substrates for electrochemical energy storage. ASC Nano 6:5531–5538
21. Guan C, Xia X, Meng N, Zeng Z, Cao X, Soci C, Zhang H, Fan HJ (2012) Hollow core-shell nanostructure supercapacitor electrodes: gap matters. Energy Environ Sci 5:9085–9090
22. Grote F, Wen L, Lei Y (2014) Nano-engineering of three-dimensional core/shell nanotube arrays for high performance supercapacitors. J Power Sources 256:37–42
23. Huang M, Zhang Y, Li F, Zhang L, Wen Z, Liu Q (2014) Facile synthesis of hierarchical Co₃O₄@MnO₂ core-shell arrays on Ni foam for asymmetric supercapacitors. J Power Sources 252:98–106
24. Huang M, Zhang Y, Li F, Wang Z, Alamusi, Hu N, Wen Z, Liu Q (2014) Merging of kirkendall growth and ostwald ripening: CuO@MnO2 core-shell architectures for asymmetric supercapacitors. Sci Rep 4:4518
25. Li Y, Peng H, Zhang C, Chu M, Xiao P, Zhang Y (2015) Branched ultra-fine nickel oxide/manganese dioxide core-shell nanosheet arrays for electrochemical capacitors. RSC Adv 5:77115–77121
26. Xu K, Li W, Liu Q, Li B, Liu X, An L, Chen Z, Zou R, Hu J (2014) Hierarchical mesoporous NiCo₂O₄@MnO₂ core-shell nanowire arrays on nickel foam for aqueous asymmetric supercapacitors. J Mater Chem A 2:4795–4802
27. Zhu L, Chang Z, Wang Y, Chen B, Zhu Y, Tang W, Wu Y (2015) Core-shell MnO₂@Fe₂O₃ nanospindles as a positive electrode for aqueous supercapacitors. J Mater Chem A 3:22066–22072
28. Lu XF, Chen XY, Zhou W, Tong YX, Li GR (2015) α-Fe₂O₃@ PANI core-shell nanowire arrays as negative electrodes for asymmetric supercapacitors. ACS Appl Mater Interfaces 7:14843–14850.

29. Zhou C, Zhang Y, Li Y, Liu J (2013) Construction of high-capacitance 3D CoO@ polypyrrole nanowire array electrode for aqueous asymmetric supercapacitor. Nano Lett 13:2078–2085

30. Zhi M, Xiang C, Li J, Li M, Wu Ni (2013) Nanostructured carbon-metal oxide composite electrodes for supercapacitors: a review. Nanoscale 5:72–88

31. Wen T, Wu XL, Zhang S, Wang X, Xu AW (2015) Core-shell carbon-coated CuO nanocomposites: a highly stable electrode material for supercapacitors and lithium-ion batteries. Chem-Asian J 10:595–601

32. Li Z, Shao Mi, Zhou L, Zhang R, Zhang C, Han J, Wei M, Evans DG, Duan X (2016) A flexible all-solid-state micro-supercapacitor based on hierarchical CuO@layered double hydroxide core-shell nanoarrays. Nano Energy 20:294–304

33. Zhang Y, Hao XD, Diao ZP, Li J, Guan YM (2014) One-pot controllable synthesis of flower-like $CoFe_2O_4$/FeOOH nanocomposites for high-performance supercapacitors. Mater Lett 123:229–234

34. Zhang X, Xiao J, Zhang X, Meng Y, Xiao D (2016) Three-dimensional Co_3O_4 nanowires@amorphous $Ni(OH)_2$ ultrathin nanosheets hierarchical structure for electrochemical energy storage. Electrochimi Acta 191:758–766

35. Tian W, Wang X, Zhi C, Zhai T, Liu D, Zhang C, Golberg D, Bando Y (2013) $Ni(OH)_2$ nanosheet @ Fe_2O_3 nanowire hybrid composite arrays for high-performance supercapacitor electrodes. Nano Energy 2:754–763

36. Jing M, Yang Y, Zhu Y, Hou H, Wu Z, Ji X (2014) An asymmetric ultracapacitors utilizing α-$Co(OH)_2$/Co_3O_4 flakes assisted by electrochemically alternatingvoltage. Electrochimi Acta 141:234–240

37. Liu R, Jiang Z, Liu Q, Zhu X, Liu L, Ni L, Shen C (2015) Novel red blood cell shaped α-Fe_2O_3 microstructures and FeO(OH) nanorods as high capacity supercapacitors. RSC Adv 5:91127–91133.

38. Liu J, Zheng M, Shi X, Zeng H, Xia H (2016) Amorphous FeOOH quantum dots assembled mesoporous film anchored on graphene nanosheets with superior electrochemical performance for supercapacitors. Adv Funct Mater 26:919–930

39. Chen K, Chen X, Xue D (2015) Hydrothermal route to crystallization of FeOOH nanorods via $FeCl_3 \cdot 6H_2O$: effect of Fe^{3+}concentration on pseudocapacitance of iron-based materials. Cryst Eng Comm 17:1906–1910

40. Shen B, Guo R, Lang J, Liu L, Liu L, Yan X (2016) A high-temperature flexible supercapacitor based on pseudocapacitive behavior of FeOOH in an ionic liquid electrolyte. J Mater Chem A 4:8316–8327

41. McIntyre NS, Zetaruk DG (1977) X-ray photoelectron spectroscopic studies of iron oxides. Anal Chem 49:1521–1529

42. Welsh ID, Sherwood PMA (1989) Photoemission and electronic structure of FeOOH: distinguishing between oxide and oxyhydroxide. Phys Rev B 40:6386

43. Wang J, Liu S, Zhang X, Liu X, Liu X, Li N, Zhao J, Li Y (2016) A high energy asymmetric supercapacitor based on flower-like $CoMoO_4$/MnO_2 heterostructures and activated carbon. Electrochimi Acta 213:663–671

44. Ning P, Duan X, Ju X, Lin X, Tong X, Pan X, Wang T, Li Q (2016) Facile synthesis of carbon nanofibers/MnO_2 nanosheets as high-performance electrodes for asymmetric supercapacitors. Electrochimi Acta 210:754–761